Journal of Power Sources xxx (xxxx) 238430

Contents lists available at ScienceDirect

Journal of Power Sources

journal homepage: www.elsevier.com/locate/jpowsour

Metal-supported solid oxide fuel cell with low temperature single *in situ* firing: fabrication, analysis, perspectives

I.S. Erilin [a, *], I.N. Burmistrov [a], E.A. Smolyanskiy [b], A.A. Solovyev [c], D.A. Gaynullina [a], E.A. Agarkova [a], S.I. Bredikhin [a]

[a] Osipyan Institute of Solid State Physics RAS, Academician Osipyan str, 2, 142432, Chernogolovka, Moscow district, Russia
[b] National Research Tomsk Polytechnic University, Lenina Avenue, 30, 634050, Tomsk, Russia
[c] Institute of High Current Electronics SB RAS, Akademichesky Avenue, 2/3, 634055, Tomsk, Russia

HIGHLIGHTS

- The metal-supported SOFC was fabricated with single *in situ* firing at 1000 °C.
- Aerosol deposition was used for fabrication of a nanostructured anode layer.
- Magnetron sputtering was used for fabrication of a gas-tight membrane.
- Polarization resistance of an anode layer is important at less than 650 °C.

GRAPHICAL ABSTRACT

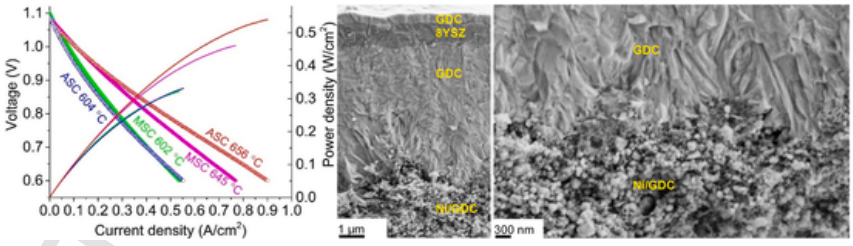

ARTICLE INFO

Keywords:
Aerosol deposition
AD
Magnetron sputtering
Metal-supported solid oxide fuel cells
MSC
In situ firing

ABSTRACT

Metal-supported solid oxide fuel cells (MSC) are the most promising fuel cells for the intermediate temperature range (500–700 °C). However, due to the necessity to consolidate ceramic layers on a metal substrate, the fabrication route is challenging and often includes tradeoffs between the desirable microstructure of the functional layers and the scalability of fabrication routes. The present study describes a manufacturable fabrication route of MSCs with desired microstructure and single *in situ* firing at 1000 °C in a testing rig imitating SOFC stack. The fabricated cell demonstrates open circuit voltage equal to 1.09–1.1 V and power density at 0.70 V equal to 0.27–0.4 W/cm^2 at 602–645 °C. The comparison to an anode-supported cell (ASC) based on a commercial anode substrate reveals that the anode of the MSC, deposited by the aerosol deposition method, has a substantial advantage over the anode of the ASC.

1. Introduction

Fuel cells are electrochemical devices that convert the chemical energy of substances to electrical energy through electrochemical reactions. Fuel cells operate in a wide temperature range from room temperature to 1000 °C [1]. The high temperatures provide a fast rate of electrochemical reactions without the need for expensive catalysts such as platinum, and the high conductivity of ion-conducting materials. Conversely, low temperatures slow all reactions, including reactions of the cell degradation, which provides an opportunity for using inexpensive materials for auxiliary elements of fuel cell stacks and generators. For many applications, the intermediate temperature range (500–700 °C) may be optimal [2–4]. Metal-supported solid oxide fuel cells (MSCs) are the most promising type of fuel cells for the intermediate temperature range as they incorporate metal supports and consequently decrease the thicknesses of the functional ceramics to the thick-

* Corresponding author.
E-mail address: ivanerilin@yandex.ru (I.S. Erilin).

https://doi.org/10.1016/j.jpowsour.2025.238430
Received 23 July 2025; Received in revised form 3 September 2025; Accepted 16 September 2025
0378-7753/

nesses necessary for the electrochemical processes, which makes them mechanically durable and relatively inexpensive. Furthermore, a metal substrate allows hermetization of the anode chamber by welding [5], which is significantly more mechanically robust than ceramic-glass sealants [6]. However, the fabrication of MSCs with the desirable microstructure of the functional layers is a challenging task. To obtain a consolidated ceramic structure, high firing temperatures, significantly exceeding 1000 °C, are often required [7–9]. The firing in air at these temperatures is detrimental to the metal supports – anode interface and the metal support itself, so the firings of the anode and electrolyte membrane better be conducted in a low-oxygen environment [7,10,11]. The firing in reducing atmosphere at high temperatures (more than 1100 °C) leads to Ni coarsening in the anode layer, which reduces the density of triple-phase boundaries (TPB) in the anode layer and negatively impacts its electrochemical activity [12,13]. High firing temperatures also lead to diffusion between the anode layer and the metal substrate, which is detrimental to the electrochemical activity of the anode layer. Moreover, the firing temperatures of anode layers, electrolyte membranes, and cathodes are usually different [14–16], which makes the whole fabrication process multi-step and time-consuming.

Currently, several well-known technological routes address the problem of ceramic consolidation in the fabrication of MSCs. Ceres Power, Ltd. incorporates laser-drilled metal substrates that are more tolerable to oxidation than a metal substrate made of powder and fabricates all major functional layers by screen printing, followed by firing at temperatures between 1000 °C and 1100 °C in air [5,17,18]. However, these temperatures may be too low to consolidate layers deposited by screen printing and still lead to low-conducting oxide film formation on the metal-anode interface [19], which does not allow to open the full potential of thin-film SOFC in terms of power density [17,18,20].

Many studies implement multistage firing in controlled atmospheres for the production of MSCs using either traditional wet-ceramic methods such as screen-printing, tape-casting, etc. [7,21,22] or combination of backbone formation and infiltration [9,16,23–25]. Though a reducing atmosphere prevents oxide film formation, these technological routes are complex and slow, as firing each cell takes hours, which is not feasible for mass production. Moreover, the infiltration technique itself is time-consuming, and wet-ceramic methods do not solve the problems of Ni agglomeration and Cr diffusion at high firing temperatures (1100–1200 °C).

Plasma spray technologies allow the formation of the whole membrane electrode assembly (MEA) without intermediate firing steps [26–28] and temperatures of post-fabrication treatment are low [26,28]. However, electrolyte membranes deposited by plasma spray technologies need to be relatively thick to maintain gas-tightness (more than 10 μm) [28–30]. Although a lot of progress has been made in improving the microstructure of SOFC electrodes deposited by plasma spray technologies [28–30] the electrodes are still characterized by relatively coarse microstructure and underdeveloped TPB in comparison to other techniques. These factors lead to relatively high resistance of the cells prepared using plasma spray technologies.

Recently, many researchers have focused on Ni-Fe alloys as materials for the substrate of MSC [31–33]. Ni-Fe alloys contain no Cr that poisons Ni-based anodes and can be easily reduced after exposure to an oxidizing atmosphere, which makes it possible to fire the whole MEA in air at high temperatures. Nevertheless, Ni-Fe alloys are brittle and difficult to weld [34–36], which eliminates one of the main advantages of MSCs and makes them similar to ASCs in terms of mechanical properties.

This study investigates a fabrication route feasible for mass production of steel-based MSC with close to an optimal structure of functional layers and single *in situ* firing in a testing rig imitating a SOFC stack at relatively low temperatures and different oxygen partial pressure on the anode and the cathode side. The fabrication route includes the dry-powder based aerosol deposition method [37–39] for deposition of an anode layer, magnetron sputtering for deposition of a three-layer electrolyte membrane [40–42], and screen-printing for deposition of a cathode layer [43]. For a more profound analysis of the electrochemical characteristics of the fabricated MSC, the anode-supported cell (ASC) with a commercial anode substrate was fabricated by our standard fabrication procedure [44] with the same cathode layer as the MSC.

2. Material and methods

Fig. 1(a) demonstrates metal substrates prepared by sintering metal powder in a vacuum furnace SNVE 1.3.1./16 (ThermoCeramics,

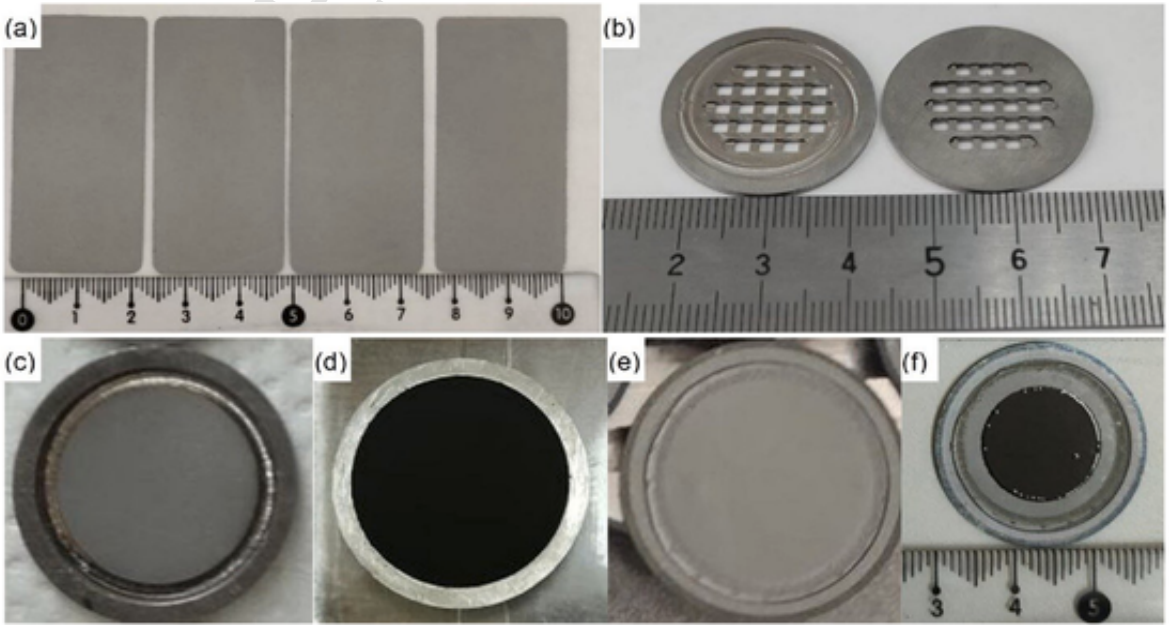

Fig. 1. (a) Metal substrates after sintering; (b) Metal frames; (c) Metal substrates welded into the metal frame; (d) Metal substrate with the deposited anode layer; (e) The cell with the Ni/GDC anode layer and the GDC-8YSZ-GDC electrolyte membrane; (f) The MSC with the cathode layer.

Russia) at 1100 °C for 1 h under 10-5 Torr pressure. The powder was produced by laser ablation of «Crofer » steel (VDM Metals GmbH, Germany) and sieved through a mesh of <20 μm. The substrates were rolled to make their surface flatter, cut into disks with a diameter of 23 mm by laser marker MiniMarker 2-M50 (CNII LOT, Russia), and then welded into « Crofer » steel frames with a grid thickness of 0.7 mm and a total thickness of 1 mm (Fig. 1(b and c)). The porosity of the substrates was determined by weighing and measuring the geometry.

Fig. 1(d) demonstrates the metal support with an anode layer. The anode layer was deposited of Ni (surface area 8.1 ± 0.5 $m^2 g^{-1}$, IEP, UB RAS, Russia) and 10 mol.% gadolinia-doped ceria (GDC) (surface area 6.1 $m^2 g^{-1}$, Kceracell Co. Ltd., South Korea) with a 50/50 wt% fraction powders by the aerosol deposition method. The self-made laboratory setup [45] includes a fluidized bed aerosol generator and a 5 mm^2 converging nozzle with axial symmetry. The absolute pressure in the deposition chamber was 200 Pa, and that in front of the nozzle was 0.1 MPa. The distance between the nozzle and the substrate was 1 cm. Dry nitrogen was used as a carrier gas with a flow rate of 35 ± 15 NLPM.

Fig. 1(e) demonstrates the cell with a three-layer GDC- 8 mol.% yttria-stabilized zirconia (8YSZ)-GDC electrolyte membrane deposited on the anode without intermediate firing steps. The membrane was prepared using the reactive magnetron sputtering method. The sputtering was carried out using metal targets with the composition Zr–Y (85:15 at.%) and Ce–Gd (90:10 at.%) (Girmet, Russia) [44]. The deposition was performed in the atmosphere of Ar/O_2 mixture at a working pressure of 0.2 Pa. The deposition rate of 8YSZ and GDC layers was 0.72 $\mu m \cdot h^{-1}$ and 2 $\mu m \cdot h^{-1}$, respectively. A thin layer of 8YSZ was incorporated into the electrolyte structure to suppress electronic conduction in the GDC in a reducing atmosphere.

Fig. 1(f) demonstrates a $(La_{0.60}Sr_{0.40})_{0.95}Co_{0.20}Fe_{0.80}O_{3-x}$ (LSCF)/GDC-LSCF (Kceracell Co. Ltd., South Korea) cathode layer that was applied by the screen printing technique. The area of the cathode was 1.77 cm^2.

The fabricated cells were subjected to *in situ* firing in a testing rig with a maximum firing temperature of 1000 °C. Nitrogen gas was on the anode side of the cell, and air was on the cathode side. The nitrogen was changed to hydrogen after cooling to 650 °C.

The ASC was based on a commercial two-layer anode support from Kceracell Co. Ltd. (South Korea) with a thickness of 700 μm (NiO/YSZ composite) [44,46] and diameter of 21 mm. The two-layer electrolyte membrane (8YSZ-GDC) was deposited by the magnetron sputtering equipment used for the MSC. The thickness of the 8YSZ and GDC layers was 5 μm and 1 μm, respectively. The anode-membrane half-cell was sintered at 1200 °C in air to stabilize the phase and crystalline structure of the membrane. The same LSCF/GDC-LSCF (Kceracell Co. Ltd., South Korea) cathode layer as for the MSC was applied by the screen-printing technique. The LSCF/GDC layer was applied onto the electrolyte membrane. After drying at 80 °C, the LSCF layer was applied onto the LSCF/GDC layer. The area of the cathode was 1.77 cm^2. The cathode layer was sintered at 1050 °C in air as recommended by Kceracell Co. Ltd.

The testing rig included metal anode and cathode current collecting/gas supply plates made of steel Crofer 22H. The steel plates in the testing rig imitate bipolar plates in a SOFC stack and have the current collecting ribs 1 mm wide and gas channels 2 mm wide parallel to a testing cell. The Ni mesh with a thickness of 0.25 mm was placed on the anode plate, and the ribs of the cathode plate were coated with the LSCF for better adhesion to the cells. Gas insulation of electrodes was provided by compression gaskets [44].

Electrochemical measurements were conducted using a potentiostat/galvanostat/ZRA Reference 3000 (Gamry Instruments, USA) with air as an oxidant and hydrogen as a fuel. Dry hydrogen was used in the case of MSC, and wet hydrogen (3 vol% H_2O) in the case of ASC. Dry anode gas is used in the case of the MSC to minimize anode-side humidity during *in situ* firing. Changing gas humidity during testing is technically infeasible in our testing rig without risking anode oxidation. Impedance spectra were collected in a frequency range from 0.1 Hz up to 300 kHz at a 20 mV voltage magnitude. The impedance spectra were fitted by using an equivalent circuit model.

The samples were studied using scanning electron microscopy (SEM) (Supra 50VP, Zeiss, Germany) with an installed energy-dispersive X-ray (EDX) spectrometer (Oxford Instruments, UK).

3. Results and discussion

Fig. 2 demonstrates SEM images of the GDC-8YSZ-GDC electrolyte membrane deposited by magnetron sputtering on the unsintered Ni/GDC anode deposited by the aerosol deposition method. Magnetron sputtering deposits films by condensing atoms. This process allows the formation of gas-tight films if parameters are chosen carefully. Fig. 2 shows that the electrolyte membrane is gas-tight after deposition.

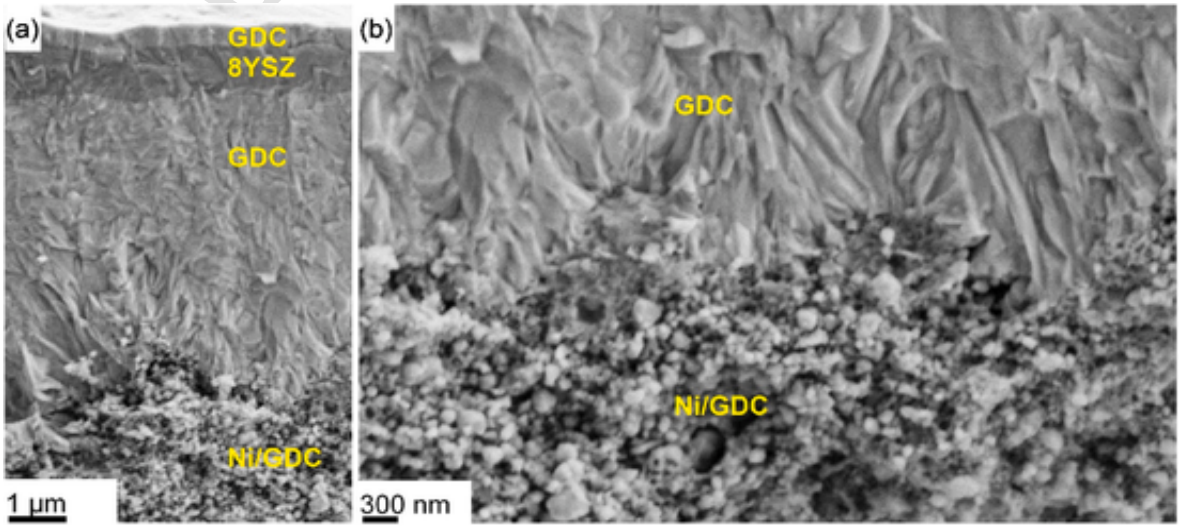

Fig. 2. (a) Cross-section of the GDC-8YSZ-GDC membrane deposited on the unsintered Ni/GDC anode; (b) Interface between the GDC layer of the membrane and the Ni/GDC anode.

High-temperature treatment of the electrolyte membrane is desirable only for stress relief and stabilization of oxygen stoichiometry [41]. The gas-tight microstructure of the membrane provides an opportunity for *in situ* firing with different gases on the anode and the cathode side. GDC electrolyte in the anode layer provides nuclei for membrane deposition, which leads to strong adhesion between the anode and the membrane even before sintering Fig. 2(b). The nano-to submicron particles are uniformly distributed throughout the layer, forming the nanostructured anode with uniform density, which provides an opportunity for obtaining consolidation of the Ni/GDC anode layer at temperatures as low as 950 °C [45]. The average ratio of Ni to GDC in the anode layer is 43/57 wt% [45].

Fig. 3 shows the SEM images of a cross-section of the MSC after testing. The thickness of the metal substrate is 300 μm (Fig. 3(a)), and the porosity is 35 ± 5 %. The Ni/GDC anode penetrates the substrate at 30–40 μm. The thickness of the anode layer relative to the top surface of the metal substrate is about several micrometers (Fig. 3(b)). This provides strong adhesion between the substrate and the anode [45] because the contact area is high compared to the thickness of the anode layer. The substrate has about 35 % porosity. Therefore, the effective thickness of the anode layer can be estimated as 35 ± 5 μm × 0.35 ± 0.05 = 12.5 ± 3.5 μm. This effective thickness should be close to optimal for electrochemical reactions on Ni/GDC anode [47], especially for a nanostructured anode with high TPB. Because the anode layer penetrates the metal substrate, the electron transport distance from the substrate to any point in the anode layer is reduced. This shorter distance allows for lower polarization resistance in the anode layer, even if the Ni content is relatively low or Ni has undergone some agglomeration. As a result, operational stability may increase. The total thickness of the electrolyte membrane (GDC-8YSZ-GDC) is 6 μm, and the 8YSZ layer is 0.9 μm (Fig. 3(c)). The optimal thickness, equal to 1 μm, of the YSZ layer deposited by magnetron sputtering was determined in our previous study for the anode-supported cell [41]. The 6 μm GDC layer provides a microstructure without visible defects. A decrease in the thickness of the GDC layer is possible, but is not justified in our opinion, as it contributes little to the total resistivity of the cell [45]. However, if the thickness of the GDC is decreased, the possibility of random defects due to metal substrate relief is increased. The total thickness of the cathode (LSCF/GDC + LSCF) layer is about 45–50 μm, where the LSCF/GDC layer is attached to the electrolyte membrane and has a thickness of about 25 μm. The electrolyte membrane has no visible delamination from the anode or the cathode layer.

Fig. 3(d) and (e) demonstrate a cathode-membrane interface and an anode-membrane interface, respectively. Solid bridges between the electrodes and the membrane are visible, which indicates good adhesion after the *in situ* firing at 1000 °C. The structures of the anode and cathode layers have submicron porosity.

Fig. 4 demonstrates elemental analysis of the cross-section of the MSC after the test. Table 1 presents the quantitative results of elemental analysis from areas marked on Fig. 4(a). Fig. 4(b) and Table 1 demonstrate that Ni and GDC are uniformly distributed in the anode layer without signs of Ni agglomeration. The Ni/GDC ratio is about

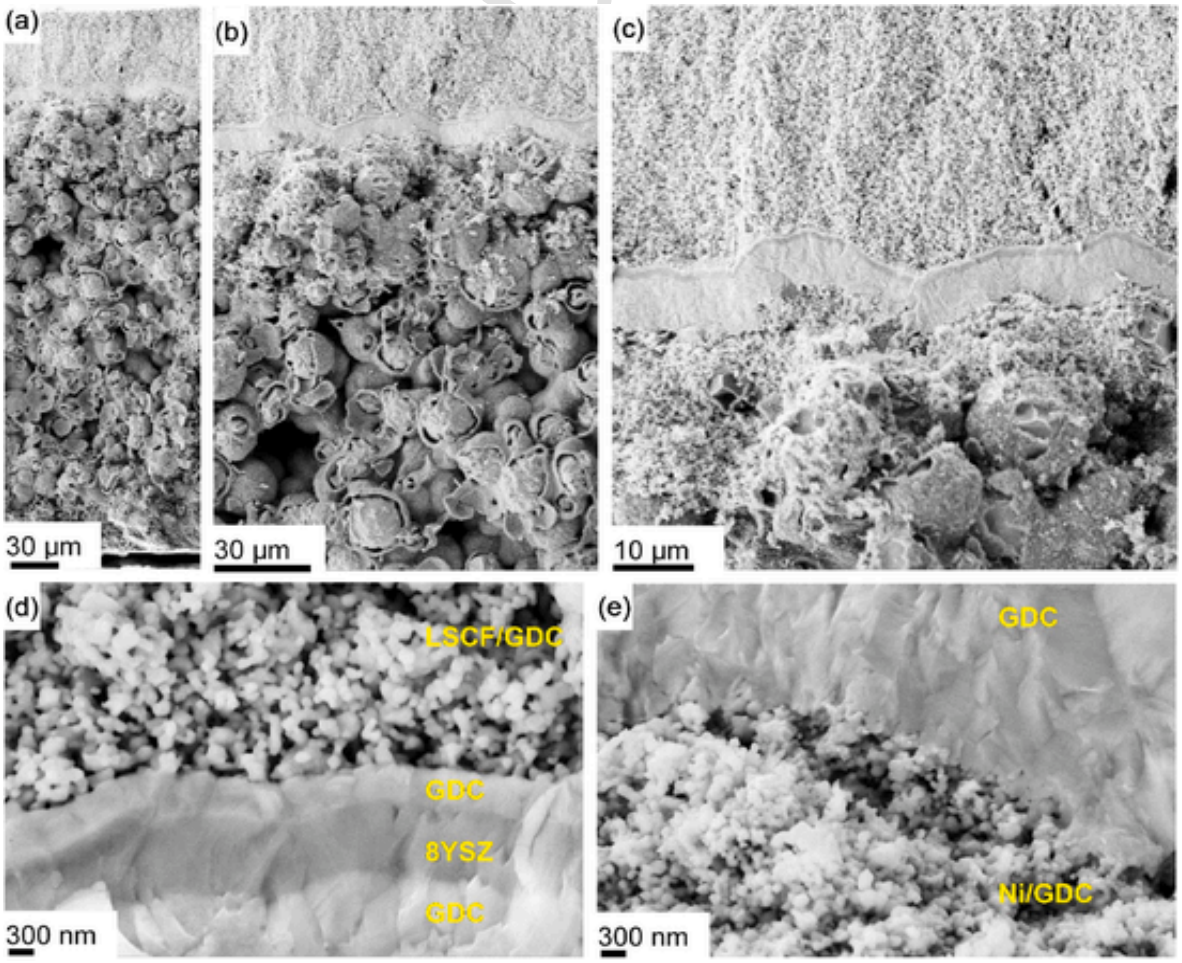

Fig. 3. SEM images of a cross-section of the MSC after testing (a) The whole cross-section; (b) Higher magnification of the upper part of the cell; (c) The membrane-electrode assembly; (d) Cathode-membrane interface; (e) Anode-membrane interface.

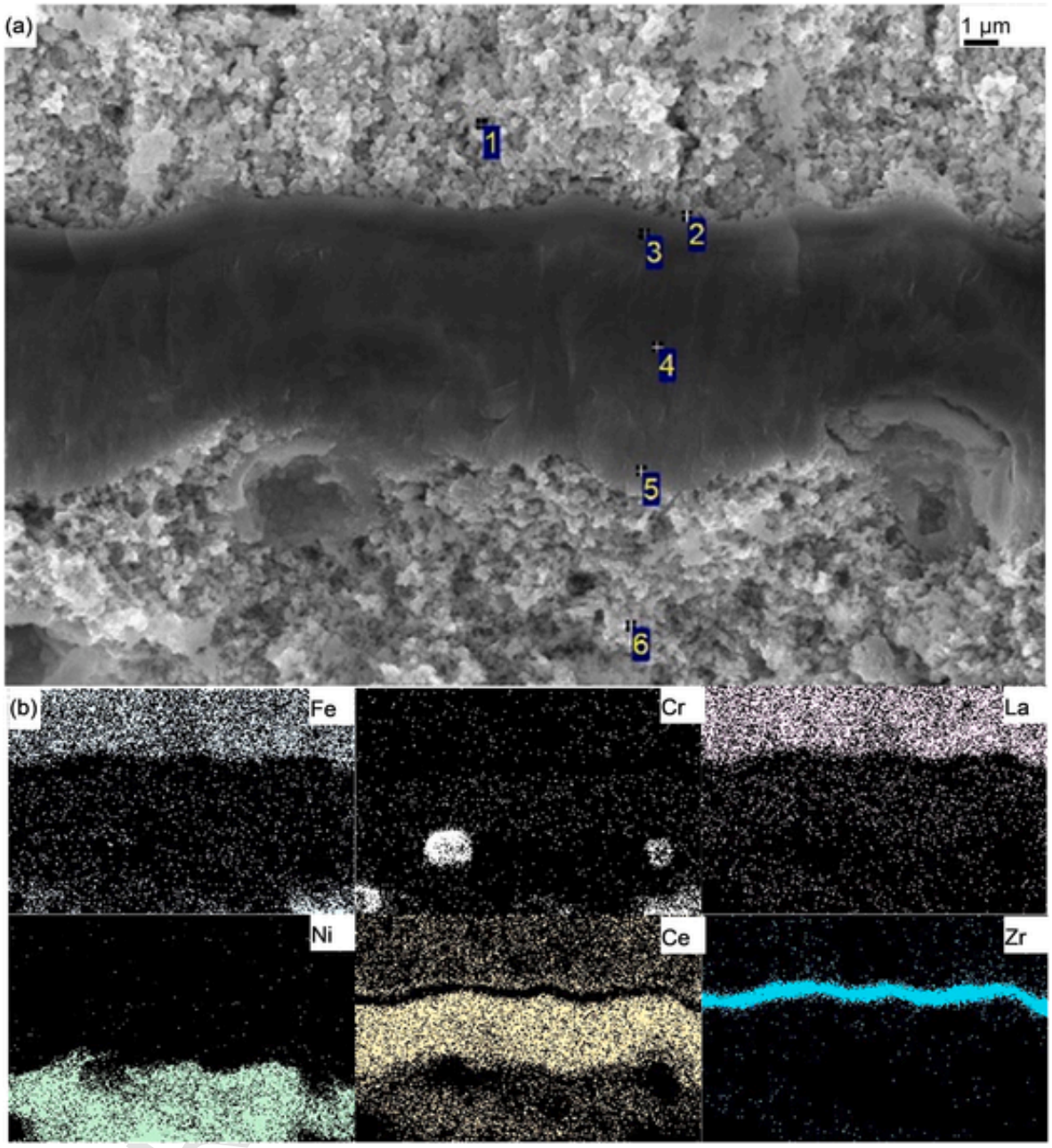

Fig. 4. SEM image (a) Cross-section of the MSC for EDX analysis after testing; (b) Corresponding mapping of Fe, Cr, La, Ni, Ce, Zr.

Table 1
Results of EDX analysis from areas marked on Fig. 4(a).

Spectrum	O	Fe	Co	Ni	Sr	Zr	La	Ce	Gd
1	14	9	3		4		19	46	5
2	28	4			4		9	47	8
3	32					31		28	9
4	20							72	8
5	18			3				69	10
6	16	3		38				38	5

All results in weight %.

42/58 wt% (spectrum 6), which is in agreement with our previous research [45]. GDC is also uniformly distributed in the cathode layer. The uniform distribution of GDC provides a developed TPB for both electrodes. Fig. 4(b) shows that the metal grains are covered with a chromia layer, which prevents further oxidation of the metal grains and keeps the high conductivity of the substrate. Table 1 demonstrates that no foreign elements were registered in the electrolyte membrane (spectra 3, 4), and Fig. 4(b) shows that there are no peculiarities in the part of the membrane adjacent to the metal grain. Table 1 proves that the thin upper GDC layer prevents contact between the YSZ electron blocking layer and LSCF (spectra 2, 3) that could have led to the formation of low-conducting phases [48]. Ultimately, no signs of microstructural degradation were registered in the MSC after the test.

Fig. 5 demonstrates the SEM images of a cross-section of the ASC after testing. The Ni/8YSZ anode support includes two layers: a coarse current-collecting layer (thickness 0.7 mm) and a fine anode functional layer (thickness 25 μm). The total thickness of the electrolyte membrane (8YSZ-GDC) is about 6 μm, and GDC is about 1 μm (Fig. 5 (b)). The membrane has a gas-tight microstructure. The total

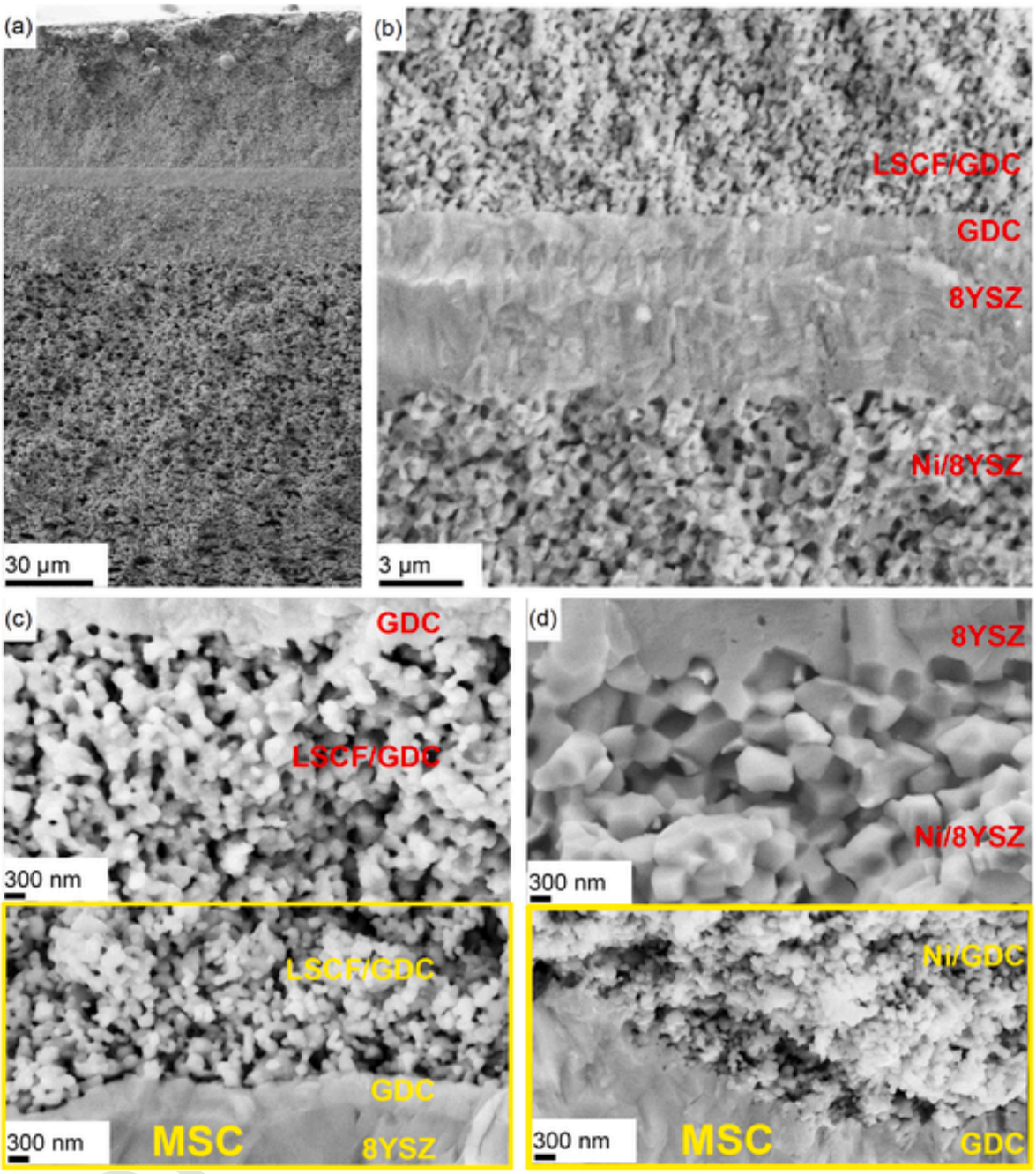

Fig. 5. SEM image (a) Cross section of the ASC after testing in low magnification; (b) Cross section of the ASC in high magnification of the MEA; (c) Cathode–membrane interface of the ASC with cathode-membrane interface of the MSC for comparison; (d) Anode–membrane interface of the ASC with anode-membrane interface of the MSC for comparison.

thickness of the cathode (LSCF/GDC + LSCF) layer is 45–50 μm, where the LSCF/GDC layer is attached to the electrolyte membrane and has a thickness of about 25 μm (Fig. 5 (a)). Fig. 5(c) shows that the difference in grain size between the cathodes of the MSC and ASC is not very significant. On the other hand, the difference in grain size between the anodes of the MSC and ASC is obvious Fig. 5(d). The significantly finer microstructure of the Ni/GDC layer provides more of the electrochemically active surfaces.

Fig. 6 demonstrates the electrochemical data of the MSC and ASC. Fig. 6(a) presents the current-voltage and current-power dependencies of the MSC and ASC. Table 2 displays values of OCV and power densities at 0.70 V and 0.90 V for the cells. The values of OCV are close to the thermodynamic values and provide direct evidence of the absence of substantial gas or electron leakages between the anode and the cathode, which indicates the gas-tightness of the electrolyte membrane and its low electronic conductivity for both cells. The closeness of the OCV to the thermodynamic values for the MSC proves that the relatively high relief of the metal substrate does not strongly affect the quality of the electrolyte membrane deposited by magnetron sputtering. The MSC has a slightly higher OCV than the ASC due to the use of dry hydrogen in the case of the MSC. Almost identical power densities for MSC and ASC at temperatures around 600 °C and different at temperatures around 650 °C imply the differences in the structure of impedances of the cells. Table 3 presents performance and technological

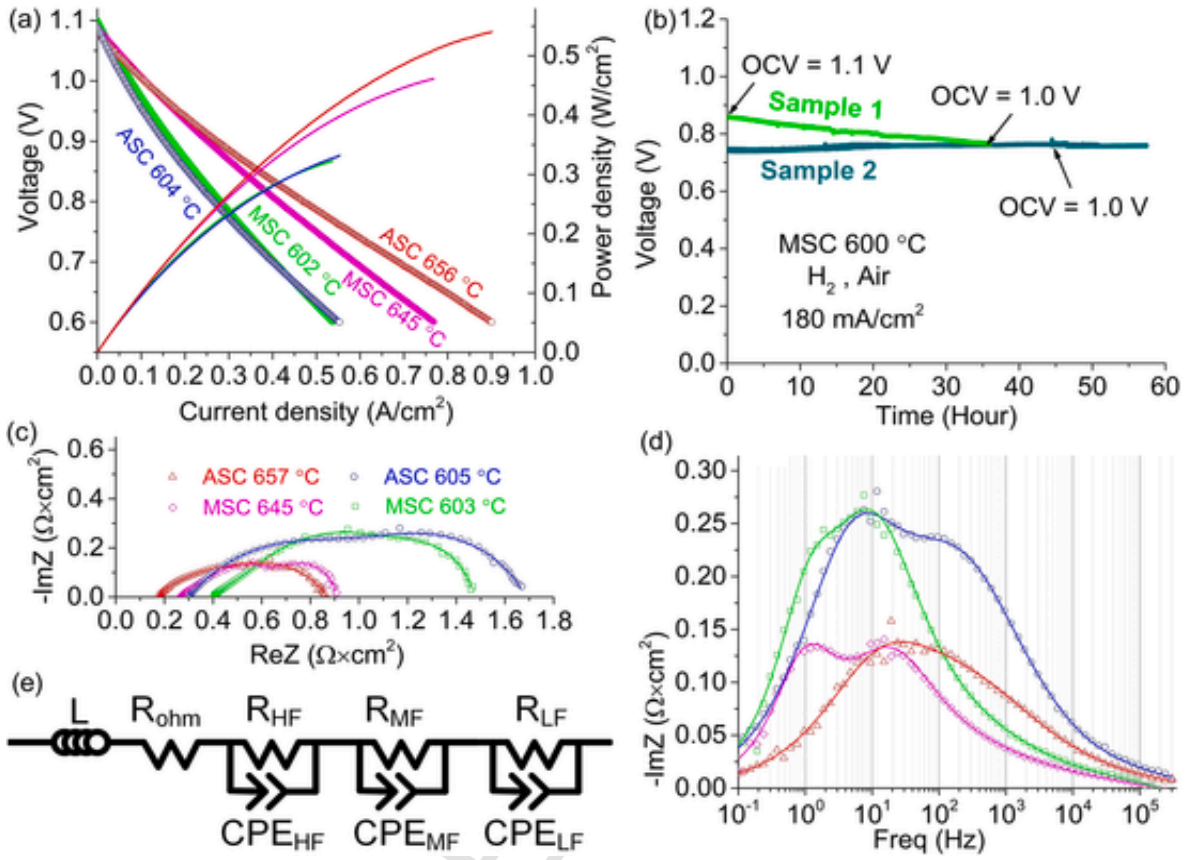

Fig. 6. (a) Current-voltage and current-power dependencies of the MSC and ASC; (b) Time dependence of the voltage for two samples of MSC with current load 180 mA/cm^2; (c) Impedance hodographs near OCV for the MSC and ASC with fits (solid lines); (d) Bode plots of the imaginary part of the impedance with fits (solid lines); (e) Equivalent circuit model for the MSC and ASC.

Table 2
OCV and power densities of the MSC and ASC.

Cell type	Temperature, °C	OCV, V	Power density, mW/cm^2	
			at 0.70 V	at 0.90 V
MSC	from 602 to 645	from 1.099 to 1.087	from 283 to 411	from 154 to 227
ASC	from 604 to 656	from 1.089 to 1.080	from 280 to 481	from 137 to 245

comparison of the fabricated in this study MSC with state-of-the-art MSCs with steel support and LSCF-based cathode. The fabricated MSC has good values of power densities for the case of LSCF-based cathodes, especially considering that the cells were tested in conditions close to conditions in stacks of SOFC in terms of gas supply and current collection. Our previous study showed that the metal support–anode–electrolyte membrane structure of the MSC can withstand thermal cycling at a heating rate of 500 °C/h without structural failure [45]. This stability results from the strong adhesion of the penetrated anode layer to the metal substrate and the magnetron-grown electrolyte membrane to the anode layer. However, the mechanical stabil-

Table 3
Performance and technological comparison of state-of-the-art MSCs with steel support and LSCF-based cathodes.

Ref.	Year	Anode	Num. of firing steps	Max. firing temp. (°C)	Atmosphere of firing	OCV		Power density at 0.9 V (W/cm2)		Power density at 0.7 V (W/cm2)	
						650 °C	600 °C	650 °C	600 °C	650 °C	600 °C
This work	2025	Ni/GDC	1 *(in situ)*	1000	N_2/Air	1.09	1.10	0.23	0.15	0.42	0.28
[29]	2025	Ni/GDC	1 *(in situ)*	800[a]	H $_2$/Air	1.04	1.05	0.14	0.07	0.31	0.19
[49]	2021	Ni/GDC	1 *(in situ)*	750[a]	H $_2$/Air	1.00	1.01	0.18	0.10	0.50	0.37
[7,13]	2020	Ni/GDC	1 + 1 *(in situ)*	1100	H_2, H $_2$/Air	1.15	1.15	0.43	0.22	0.80	0.45
[9]	2018	Ni/LST-GDC	5	1000	Air	1.16	1.17	0.13	0.10	0.20	0.15
[17,20]	2017	Ni/GDC	Not stated	1000–1100	Air	–	1.10	–	–	–	0.29 (0.75 V)
[50]	2016	Ni/ScSz	1 *(in situ)*	750[a]	H $_2$/Air	0.95	0.95	0.11	0.09	0.65	0.50

[a] The cells were formed by plasma spray technology.

ity of the cathode layer during rapid thermal cycling remains a problem that needs to be addressed in further research.

Fig. 6(b) demonstrates the short-term operation stability of the MSCs in a galvanostatic regime at 600 °C for two samples with different OCV under the same current density. The sample with an initial OCV of 1.1 V exhibited degradation due to the drop in OCV, but there was no increase in resistivity. The sample with initial OCV of 1.0 V demonstrated no degradation. The lower OCV indicates more water (oxygen) on the anode side, which is due to problems with hermitization of the testing rig or defects in the membrane. Therefore, different amounts of oxygen or humidification during *in situ* firing and testing could play a role in the difference in stability of the samples. However, there is no explanation of the exact mechanism of OCV degradation, and additional research is needed. Fig. 6(c) demonstrates hodographs of the impedance measured under OCV conditions with plotted fits. Fig. 6(d) demonstrates Bode plots of the imaginary part of the measured impedances with plotted fits. Fig. 6(e) shows an equivalent circuit model (L – inductor; R_{ohm}, R_{HF}, R_{MF}, R_{LF} resistors; CPE_{HF}, CPE_{MF}, CPE_{LF} – constant phase elements). According to the equivalent circuit, L and R_{ohm} are responsible for the inductance of the supply wires and ohmic losses of the cell, respectively. As will be shown below, (R_{HF}-CPE_{HF}) includes the most dominant contribution to the polarization of anode reactions, (R_{MF}-CPE_{MF}) – of cathode reactions, and (R_{LF}-CPE_{LF}) – of mass-transport losses in the case of low fuel humidity. The distinct contributions to the impedances of the cells were separated by fitting and presented in Fig. 7 for qualitative analysis.

The higher ohmic losses of the MSC may come from several reasons, such as the presence of low conducting films at the anode-metal substrate interface, the less sintered cathode, and poor phase or crystal structure of the magnetron-sputtered membrane due to the lower firing temperature than in the case of ASC. The difference between the ohmic losses of the MSC and ASC displays no temperature dependency (0.1 Ω × cm^2 at 600–650 °C), which may indicate that the additional ohmic losses are associated with the electronic current. In our previous study [45], we used $(La_{0.80}Sr_{0.20})_{0.95}CoO_{3-\delta}$ (LSC) cathode and the metal substrate with Ni protective coating for a MSC mini stack with single *in situ* firing at 950 °C. The mini stack demonstrated significantly better values of the ohmic resistance despite the lower firing temperature of the anode layer, which points out the ways for improvements.

Fig. 7 demonstrates the Bode plots of the imaginary part of the impedance with separated R-CPE contributions for the MSC and ASC at 600–650 °C. Fig. 8 demonstrates column plots of the real part of the contributions to the impedance of the MSC and ASC at 600–650 °C with fitting error bars.

The magnitude of -ImZ and ReZ of middle-frequency contributions (R_{MF}-CPE_{MF}) with resonance at 5–20 Hz are close and increase in the same ratio for the MSC and ASC, which provides evidence for mostly the same nature of these contributions. The most dominant role in these contributions probably corresponds to processes of the similar LSCF-based cathode layer, which is consistent with the frequency range from literature data [51–55]. The different resonance frequencies of the peaks of the cathode contribution for the MSC and ASC can be explained by different sintering temperatures of the LSCF [55,56] by other contributions to this frequency range for the ASC and the MSC, or by fitting errors. This contribution was not observed in our study of the MSC with the LSC cathode and single GDC membrane due to different cathode material [45].

The low-frequency contribution (R_{LF}-CPE_{LF}) with peaks at 1 Hz in the case of the MSC exhibits weak thermal activation behavior (Figs. 7 and 8) and is likely linked to gas-conversion impedance. The gas-conversion impedance is most likely caused by low humidity on the anode side [57–60] exacerbated by the high chemical capacitance of GDC due to changes in oxygen stoichiometry [61]. This contribution was not observed in our study of the MSC with the LSC cathode and single GDC membrane [45] due to high humidity on the anode side. The absence of the low-frequency peak in the case of the ASC can be explained by the absence of the GDC in the anode layer and the higher humidity of the anode gas.

The polarization losses of the MSC are lower than that of the ASC, and the lower the temperature, the more the difference (Fig. 6), which provides lower total losses in the case of the MSC at 600 °C despite its higher ohmic losses. It is visible from the bode plot (Fig. 6(d)) as well as from the fits (Fig. 7) that the difference in polarization losses for the MSC and ASC comes from the contribution to the impedance in the high-frequency range (R_{HF}-CPE_{HF}) with resonance frequency at about 100–500 Hz in the case of ASC, which corresponds to processes on the YSZ/Ni fuel electrode of SOFCs [51,57,62–64]. The anode for the MSC was fabricated from the powder with nano Ni and submicron GDC particle size and sintered at a relatively low temperature of 1000 °C, which led to high TPB values. The high TPB values of the anode layer of the MSC and higher ionic as well as electronic conductivity of GDC that extends electrochemical reaction to the double phase boundary lead to significantly lower anode polarization losses than in the case of the ASC, which is especially important at temperatures less than 650 °C, where anode contributions to the losses are significant. [57,65]. Fig. 8 shows the YSZ/Ni anode contribution to the impedance of the ASC is indeed comparable to or even higher than that of the LSCF/GDC-LSCF cathode. Moreover, some anode processes probably also contribute to the MF range, which makes anode contribution to the impedance even more significant. Therefore, the polarization resistance of the cathode layer in the case of the ASC is less influential than in the case of the MSC

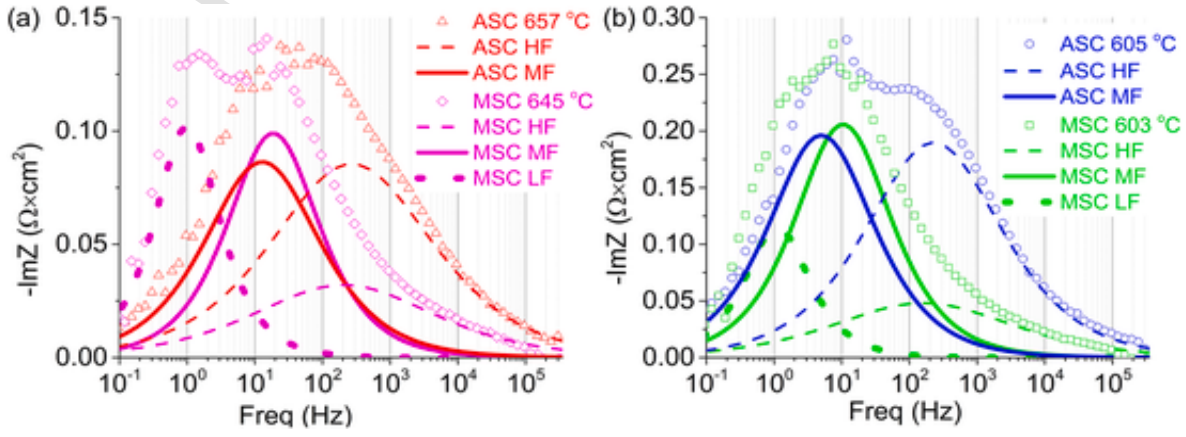

Fig. 7. Bode plots of the imaginary part of the impedance with separated R-CPE contributions for the MSC and ASC at (a) around 650 °C; (b) around 600 °C.

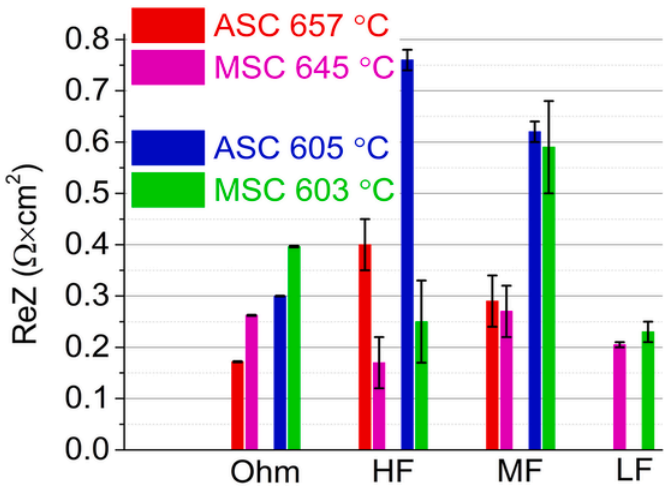

Fig. 8. Column plots of the real part of the contributions to the impedance of the MSC and ASC at 600–650 °C with fitting error bars.

because the polarization resistance of the anode layer of the ASC is also a significant factor limiting cell performance.

The difference in power densities for MSC and ASC at 650 °C increases with increasing current. However, at high voltages such as 0.9 V, that is, at high electrical efficiency, the power densities of MSC and ASC are close (Table 2), which is due to high activation barriers for electrode reactions at low currents. Therefore, the high activity of the anode layer in the case of MSC is especially important when operating at high electrical efficiency.

Despite the high activity of the anode layer in case of the MSC, the polarization losses are still much higher than in the case of our MSC with LSC cathode [42,45], which indicates that for unlocking the full potential of the MSC the significant improvement in cathode activity in comparison to the commercial LSCF-based cathode (Kceracell Co. Ltd.) is needed. The use of LSC cathode fabricated by screen printing is not a reliable solution for practical purposes due to its high coefficient of thermal expansion of 20 K^{-1} [66]. A way to improve the cathode activity is to find new materials or fabricate the existing cathode materials with superior microstructure and low sintering temperatures. The possible options for obtaining cathode layers of conventional materials with superior microstructure may include fabrication of the thin LSC cathode by magnetron sputtering [67], or by aerosol deposition method, significant improvement in TPB values of the LSCF-based cathodes fabricated by AD [68], screen printing or other powder-based methods.

4. Conclusions

The fabrication of the MSC with single *in situ* firing of all functional layers at 1000 °C was described. The fabrication included the deposition of the Ni/GDC anode by the aerosol deposition method, the GDC-8YSZ-GDC electrolyte membrane by magnetron sputtering, and the LSCF/GDC-LSCF cathode layer by screen printing. The MSC demonstrated OCV of 1.099–1.087 V and power density of 283–411 mW/cm^2 at 0.7 V and 602–645 °C.

The high adhesion between separate particles in the unsintered anode layer allows the electrolyte membrane deposition by magnetron sputtering without intermediate firing. The initial gas-tightness of the membrane provides gas separation between the anode and the cathode chambers. In the anode layer, the small size of powder particles (<100 nm) not bonded in agglomerates due to the absence of liquids in the fabrication process provides low sintering temperatures. These facts make it possible to fire all functional layers of MSC simultaneously in a desired gas atmosphere inside the testing rig imitating SOFC stack.

The MSC demonstrated less polarization resistance than the ASC in a high-frequency region from about 10 Hz to 100 kHz, which is explained by the highly developed TPB of the Ni/GDC anode deposited by aerosol deposition method as well as by high electronic and ionic conductivity of GDC. The polarization resistance of the anode layer in the case of the ASC is at least as significant as the polarization resistance of the LSCF/GDC-LSCF cathode layer. However, the polarization resistance of the LSCF/GDC-LSCF cathode layer in the case of the MSC is the most significant factor impeding the cell performance. The high activity of the anode layer is especially important when operating at high voltages, that is, at high electrical efficiency. To express the full potential of the MSC, an increase in cathode activity is needed, which can be obtained by new materials or by significant microstructure improvement of the existing ones.

CRediT authorship contribution statement

I.S. Erilin: Writing – original draft, Visualization, Methodology, Investigation, Data curation, Conceptualization. **I.N. Burmistrov:** Writing – review & editing, Methodology, Data curation, Conceptualization. **E.A. Smolyanskiy:** Investigation, Data curation. **A.A. Solovyev:** Writing – review & editing, Methodology, Investigation, Data curation. **D.A. Gaynullina:** Investigation. **E.A. Agarkova:** Methodology. **S.I. Bredikhin:** Supervision, Methodology.

Declaration of competing interest

The authors declare that they have no known competing financial interests or personal relationships that could have appeared to influence the work reported in this paper.

Acknowledgements

Authors acknowledge support of the Research Facility Center at the ISSP RAS in the part of scanning microscopy studies.

Data availability

Data will be made available on request.

References

[1] L. Fan, Z. Tu, S.H. Chan, Recent development of hydrogen and fuel cell technologies: a review, Energy Rep. 7 (2021) 8421–8446, https://doi.org/10.1016/j.egyr.2021.08.003.
[2] D.J. Brett, A. Atkinson, N.P. Brandon, S.J. Skinner, Intermediate temperature solid oxide fuel cells, Chem. Soc. Rev. 37 (8) (2008) 1568–1578, https://doi.org/10.1039/b612060c.
[3] H. Su, Y.H. Hu, Progress in low-temperature solid oxide fuel cells with hydrocarbon fuels, Chem. Eng. J. 402 (2020) 126235, https://doi.org/10.1016/j.cej.2020.126235.
[4] J. Huang, F. Xie, C. Wang, Z. Mao, Development of solid oxide fuel cell materials for intermediate-to-low temperature operation, Int. J. Hydrogen Energy 37 (1) (2012) 877–883, https://doi.org/10.1016/j.ijhydene.2011.04.030.
[5] R.T. Leah, A. Bone, E. Hammer, A. Selcuk, M. Rahman, A. Clare, M. Selby, Development progress on the ceres power steel cell technology platform: further progress towards commercialization, ECS Trans. 78 (1) (2017) 87, https://doi.org/10.1149/07801.0087ecst.
[6] J. Bae, A novel metal supported SOFC fabrication method developed in KAIST: a sinter-joining method, J. Korean Ceram. Soc. 53 (5) (2016) 478–482, https://doi.org/10.4191/kcers.2016.53.5.478.
[7] D. Udomsilp, J. Rechberger, R. Neubauer, C. Bischof, F. Thaler, W. Schafbauer, M. Bram, Metal-supported solid oxide fuel cells with exceptionally high power density for range extender systems, Cell Rep. Phys. Sci. 1 (6) (2020), https://doi.org/10.1016/j.xcrp.2020.100072.
[8] Z. Ruhma, K. Yashiro, I. Oikawa, H. Takamura, T. Kawada, Metal-supported SOFC fabricated by tape casting and its characterization: a study of the Co-sintering process, J. Eng. Technol. Sci. 53 (5) (2021), https://doi.org/10.5614/j.eng.technol.sci.2021.53.5.11.

[9] K. Lee, J. Kang, J. Lee, S. Lee, J. Bae, Evaluation of metal-supported solid oxide fuel cells (MS-SOFCs) fabricated at low temperature (~ 1,000 C) using wet chemical coating processes and a catalyst wet impregnation method, Int. J. Hydrogen Energy 43 (7) (2018) 3786–3796, https://doi.org/10.1016/j.ijhydene.2018.01.027.
[10] V.V. Krishnan, Recent developments in metal-supported solid oxide fuel cells, Wiley Interdiscipl. Rev.: Energy Environ. 6 (5) (2017) e246, https://doi.org/10.1002/wene.246.
[11] H. Lv, Z. Huang, G. Zhang, T. Chen, S. Wang, A new design of metal supported micro-tubular solid oxide fuel cell with sandwich structure, Int. J. Hydrogen Energy 47 (78) (2022) 33420–33428, https://doi.org/10.1016/j.ijhydene.2022.07.218.
[12] M.C. Tucker, Progress in metal-supported solid oxide fuel cells: a review, J. Power Sources 195 (15) (2010) 4570–4582, https://doi.org/10.1016/j.jpowsour.2010.02.035.
[13] C. Bischof, A. Nenning, A. Malleier, L. Martetschläger, A. Gladbach, W. Schafbauer, M. Bram, Microstructure optimization of nickel/gadolinium-doped ceria anodes as key to significantly increasing power density of metal-supported solid oxide fuel cells, Int. J. Hydrogen Energy 44 (59) (2019) 31475–31487, https://doi.org/10.1016/j.ijhydene.2019.10.010.
[14] H.J. Cho, K.J. Kim, Y.M. Park, G.M. Choi, Flexible solid oxide fuel cells supported on thin and porous metal, Int. J. Hydrogen Energy 41 (22) (2016) 9577–9584, https://doi.org/10.1016/j.ijhydene.2016.04.040.
[15] P. Satardekar, D. Montinaro, V.M. Sglavo, Fe-doped YSZ electrolyte for the fabrication of metal supported-SOFC by co-sintering, Ceram. Int. 41 (8) (2015) 9806–9812, https://doi.org/10.1016/j.ceramint.2015.04.053.
[16] P. Blennow, J. Hjelm, T. Klemensø, S. Ramousse, A. Kromp, A. Leonide, A. Weber, Manufacturing and characterization of metal-supported solid oxide fuel cells, J. Power Sources 196 (17) (2011) 7117–7125, https://doi.org/10.1016/j.jpowsour.2010.08.088.
[17] R.T. Leah, A. Bone, A. Selcuk, D. Corcoran, M. Lankin, Z. Dehaney-Steven, P. Whalen, Development of highly robust, volume-manufacturable metal-supported SOFCs for operation below 600, ECS Trans. 35 (1) (2011) 351, https://doi.org/10.1149/1.3570010.
[18] R. Leah, A. Bone, M. Lankin, A. Selcuk, R. Pierce, L. Rees, S. Mukerjee, Low-cost, redox-stable, low-temperature SOFC developed by ceres power for multiple applications: latest development update, ECS Trans. 57 (1) (2013) 461, https://doi.org/10.1149/05701.0461ecst.
[19] C. Cadigan, C. Chmura, G. Floerchinger, P. Frankl, S. Hunt, S. Jensen, N.P. Sullivan, Performance characterization of metal-supported solid-oxide fuel cell stacks at elevated pressure, J. Power Sources 573 (2023) 233083, https://doi.org/10.1016/j.jpowsour.2023.233083.
[20] R.T. Leah, A. Bone, E. Hammer, A. Selcuk, M. Rahman, A. Clare, M. Selby, Development of high efficiency steel cell technology for multiple applications, ECS Trans. 78 (1) (2017) 2005, https://doi.org/10.1149/07801.2005ecst.
[21] V.A. Rojek-Wöckner, A.K. Opitz, M. Brandner, J. Mathé, M. Bram, A novel Ni/ceria-based anode for metal-supported solid oxide fuel cells, J. Power Sources 328 (2016) 65–74, https://doi.org/10.1016/j.jpowsour.2016.07.075.
[22] Y. Yamaguchi, H. Sumi, H. Takahashi, R. Mori, H. Shimizu, Development of metal-supported planar SOFCs fabricated by all wet process on metallurgical porous substrates, ECS Trans. 91 (1) (2019) 909, https://doi.org/10.1149/09101.0909ecst.
[23] E. Dogdibegovic, R. Wang, G.Y. Lau, M.C. Tucker, High performance metal-supported solid oxide fuel cells with infiltrated electrodes, J. Power Sources 410 (2019) 91–98, https://doi.org/10.1016/j.jpowsour.2018.11.004.
[24] A. Hagen, X. Sun, B.R. Sudireddy, Å.H. Persson, Metal supported SOFCs for mobile applications using hydrocarbon fuels, J. Electrochem. Soc. 167 (10) (2020) 104510, https://doi.org/10.1149/1945-7111/ab9b9d.
[25] M.M. Welander, B. Hu, S. Belko, K.X. Lee, P.K. Dubey, I. Robinson, M.C. Tucker, Direct utilization of gaseous fuels in metal supported solid oxide fuel cells, Int. J. Hydrogen Energy 48 (4) (2023) 1533–1539, https://doi.org/10.1016/j.ijhydene.2022.10.008.
[26] C.H. Tsai, C.S. Yang, C. Chang, C.Y. Fu, M.F. Han, S.H. Wu, Characterization of thin metal-supported solid oxide fuel cells fabricated through atmospheric Plasma spraying, Fuel Cells 23 (4) (2023) 292–303, https://doi.org/10.1002/fuce.202200205.
[27] J.T. Gao, J.H. Li, Y.P. Wang, C.J. Li, C.X. Li, Performance and stability of plasma-sprayed 10× 10 Cm 2 self-sealing metal-supported solid oxide fuel cells, J. Therm. Spray Technol. 30 (2021) 1059–1068, https://doi.org/10.1007/s11666-021-01171-5.
[28] K. Du, C. Song, B. Yuan, T. Liu, K. Wen, X. Fan, H. Liao, Plasma-sprayed dense yttria-stabilized zirconia electrolyte for metal-supported solid oxide fuel cells, Ceram. Int. 51 (7) (2025) 9412–9420, https://doi.org/10.1016/j.ceramint.2024.12.374.
[29] G. Yu, S. Chen, L. Min, W. Kui, L. Taikai, Z. Liangzhu, L. Hanlin, Development of NiO-GDC anode by atmospheric plasma spraying for metal-supported SOFCs, J. Therm. Spray Technol. 34 (1) (2025) 291–299, https://doi.org/10.1007/s11666-024-01861-w.
[30] C.S. Hwang, C.H. Tsai, C.L. Chang, C.M. Chuang, Z.Y.C. Shie, S.W. Cheng, S.H. Wu, Plasma sprayed metal-supported solid oxide fuel cell and stack with nanostructured anodes and diffusion barrier layer, Thin Solid Films 570 (2014) 183–188, https://doi.org/10.1016/j.tsf.2014.02.034.
[31] B. Zhou, Y. Chen, W. Tang, X. Zhao, H. Tao, Z. Chen, L. Zhu, High performance metal-supported solid oxide fuel cells with Ni–Fe alloy support, Int. J. Hydrogen Energy 119 (2025) 150–160, https://doi.org/10.1016/j.ijhydene.2025.03.240.
[32] X. Liu, P. Lin, J. Qian, H. Zhang, N. Ai, C. Guan, K. Chen, Modulating the structural stability of NiFe metal-supported solid oxide fuel cells, Int. J. Hydrogen Energy 114 (2025) 1–8, https://doi.org/10.1016/j.ijhydene.2025.03.021.
[33] K. Li, X. Wang, L. Jia, D. Yan, J. Pu, B. Chi, L. Jian, High performance Ni–Fe alloy supported SOFCs fabricated by low cost tape casting-screen printing-cofiring process, Int. J. Hydrogen Energy 39 (34) (2014) 19747–19752, https://doi.org/10.1016/j.ijhydene.2014.09.146.
[34] J. Adamiec, A. Grabowski, A. Lisiecki, Joining of an Ni-Al alloy by means of laser beam welding, Laser Technol. VII: Appl. Lasers 5229 (2003, October) 215–218 https://doi.org/10.1117/12.520719, SPIE.
[35] M.L. Santella, S.A. David, C.L. White, Weldability of Ni3Al-Type aluminide alloys, in: MRS Online Proceedings Library (OPL), vol. 39, 1984, p. 495, https://doi.org/10.1557/PROC-39-495.
[36] Q. Li, X. Wang, C. Liu, X. Yang, C. Li, L. Jia, J. Li, A direct-methane solid oxide fuel cell with a functionally engineered Ni–Fe metal support, J. Power Sources 537 (2022) 231533, https://doi.org/10.1016/j.jpowsour.2022.231533.
[37] I.S. Erilin, I.N. Burmistrov, D.A. Agarkov, E.A. Agarkova, D.V. Yalovenko, A.A. Solovyev, S.I. Bredikhin, Aerosol deposition of anode functional layer for metal-supported solid oxide fuel cells, Mater. Lett. 306 (2022) 130924, https://doi.org/10.1016/j.matlet.2021.130924.
[38] K. Manabe, M. Echigo, Y. Tsuda, K. Minami, J. Akedo, H. Ohnishi, Formation of dense yttria-stabilized zirconia thin film by aerosol deposition method for metal-supported solid oxide fuel cell applications, J. Chem. Eng. Jpn. 56 (1) (2023) 2261771, https://doi.org/10.1080/00219592.2023.2261771.
[39] J.J. Choi, J. Ryu, B.D. Hahn, C.W. Ahn, J.W. Kim, W.H. Yoon, D.S. Park, Low temperature preparation and characterization of solid oxide fuel cells on FeCr-based alloy support by aerosol deposition, Int. J. Hydrogen Energy 39 (24) (2014) 12878–12883, https://doi.org/10.1016/j.ijhydene.2014.06.070.
[40] F. Liang, J. Yang, H. Wang, J. Wu, Fabrication of Gd2 O3 -doped CeO2 thin films through DC reactive sputtering and their application in solid oxide fuel cells, Int. J. Miner. Metall. Mater. 30 (6) (2023) 1190–1197, https://doi.org/10.1007/s12613-023-2620-y.
[41] A. Solovyev, A. Shipilova, E. Smolyanskiy, Solid oxide fuel cells with magnetron sputtered single-layer SDC and multilayer SDC/YSZ/SDC electrolytes, Membranes 13 (6) (2023) 585, https://doi.org/10.3390/membranes13060585.
[42] I.S. Erilin, M.N. Levin, I.N. Burmistrov, D.V. Yalovenko, E.A. Smolyanskiy, A.A. Solovyev, S.I. Bredikhin, Fabrication of metal-supported solid oxide fuel cells by combining aerosol deposition and magnetron sputtering techniques, J. Solid State Electrochem. 28 (6) (2024) 1971–1976, https://doi.org/10.1007/s10008-023-05779-1.
[43] N.A. Baharuddin, N.F. Abdul Rahman, H. Abd Rahman, M.R. Somalu, M.A. Azmi, J. Raharjo, Fabrication of high-quality electrode films for solid oxide fuel cell by screen printing: a review on important processing parameters, Int. J. Energy Res. 44 (11) (2020) 8296–8313, https://doi.org/10.1002/er.5518.
[44] A. Solovyev, I.N. Burmistrov, S. Rabotkin, A. Shipilova, D.V. Yalovenko, V. Semenov, S.I. Bredikhin, Electrochemical characterization of intermediate-temperature solid oxide fuel cells with pvd-coated electrolyte, ECS Trans. 103 (1) (2021) 105, https://doi.org/10.1149/10301.0105ecst.
[45] I.S. Erilin, I.N. Burmistrov, E.A. Smolyanskiy, A.A. Solovyev, O.V. Pikalov, M.N. Levin, S.I. Bredikhin, Metal-supported solid oxide fuel cell mini-stack with single in situ firing at 950° C, Mater. Sci. Eng., B 318 (2025) 118260, https://doi.org/10.1016/j.mseb.2025.118260.
[46] A.A. Solovyev, A.V. Shipilova, S.V. Rabotkin, N.M. Bogdanovich, E.Y. Pikalova, Study of the efficiency of composite LaNi0. 6Fe0. 4O3-based cathodes in intermediate-temperature anode-supported SOFCs, Int. J. Hydrogen Energy 48 (59) (2023) 22594–22609, https://doi.org/10.1016/j.ijhydene.2023.02.011.
[47] A. Nenning, C. Bischof, J. Fleig, M. Bram, A.K. Opitz, The relation of microstructure, materials properties and impedance of SOFC electrodes: a case study of Ni/GDC anodes, Energies 13 (4) (2020) 987, https://doi.org/10.3390/en13040987.
[48] F. Wang, M. Nishi, M.E. Brito, H. Kishimoto, K. Yamaji, H. Yokokawa, T. Horita, Sr and Zr diffusion in LSCF/10GDC/8YSZ triplets for solid oxide fuel cells (SOFCs), J. Power Sources 258 (2014) 281–289, https://doi.org/10.1016/j.jpowsour.2014.02.046.
[49] Y.P. Wang, J.T. Gao, J.H. Li, C.J. Li, C.X. Li, Preparation of bulk-like La0. 8Sr0. 2Ga0. 8Mg0. 2O3-δ coatings for porous metal-supported solid oxide fuel cells via plasma spraying at increased particle temperatures, Int. J. Hydrogen Energy 46 (64) (2021) 32655–32664, https://doi.org/10.1016/j.ijhydene.2021.07.121.
[50] S.L. Zhang, H.X. Yu, C.X. Li, S.Y. Lai, C.J. Li, G.J. Yang, M. Liu, Thermally sprayed high-performance porous metal-supported solid oxide fuel cells with nanostructured La 0.6 Sr 0.4 Co 0.2 Fe 0.8 O 3− δ cathodes, J. Mater. Chem. A 4 (19) (2016) 7461–7468, https://doi.org/10.1039/C6TA02065H.
[51] J. Kim, D. Shin, J.W. Son, J.H. Lee, B.K. Kim, H.J. Je, K.J. Yoon, Fabrication and characterization of all-ceramic solid oxide fuel cells based on composite oxide anode, J. Power Sources 241 (2013) 440–448, https://doi.org/10.1016/j.jpowsour.2013.04.139.
[52] G.D. Han, K.C. Neoh, K. Bae, H.J. Choi, S.W. Park, J.W. Son, J.H. Shim, Fabrication of lanthanum strontium cobalt ferrite (LSCF) cathodes for high performance solid oxide fuel cells using a low price commercial inkjet printer, J. Power Sources 306 (2016) 503–509, https://doi.org/10.1016/j.jpowsour.2015.12.067.
[53] J.G. Lee, M.G. Park, J.H. Park, Y.G. Shul, Electrochemical characteristics of electrospun La0. 6Sr0. 4Co0. 2Fe0. 8O3− δ-Gd0. 1Ce0. 9O1. 95 cathode, Ceram. Int. 40 (6) (2014) 8053–8060, https://doi.org/10.1016/j.ceramint.2013.12.158.
[54] E. Effori, J. Laurencin, E.D.R. Silva, M. Hubert, T. David, M. Petitjean, E. Siebert, An elementary kinetic model for the LSCF and LSCF-CGO electrodes of solid oxide cells: impact of operating conditions and degradation on the electrode response, J. Electrochem. Soc. 168 (4) (2021) 044520, https://doi.org/10.1149/1945-7111/

abf40a.
[55] Ö. Çelikbilek, E. Siebert, D. Jauffrès, C.L. Martin, E. Djurado, Influence of sintering temperature on morphology and electrochemical performance of LSCF/GDC composite films as efficient cathode for SOFC, Electrochim. Acta 246 (2017) 1248–1258, https://doi.org/10.1016/j.electacta.2017.06.070.
[56] G. DiGiuseppe, D. Thompson, C. Gumeci, A.M. Hussain, N. Dale, Distribution of relaxation times analysis and interfacial effects of LSCF fired at different temperatures, Int. J. Hydrogen Energy 44 (49) (2019) 27067–27078, https://doi.org/10.1016/j.ijhydene.2019.08.160.
[57] D. Montinaro, A.R. Contino, A. Dellai, M. Rolland, Determination of the impedance contributions in anode supported solid oxide fuel cells with (La, Sr)(Co, Fe) O3– δ cathode, Int. J. Hydrogen Energy 39 (36) (2014) 21638–21646, https://doi.org/10.1016/j.ijhydene.2014.09.081.
[58] R. Mohammadi, M. Ghassemi, Y.M. Barzi, J. Pirkandi, The effect of mass transfer on electrochemical impedance of a solid oxide fuel cell anode, J. Solid State Electrochem. 18 (2014) 2815–2827, https://doi.org/10.1007/s10008-014-2536-6.
[59] S. Koomson, C.G. Lee, Effect of water on the anodic overpotential at low currents in a solid oxide fuel cell, J. Electroanal. Chem. 882 (2021) 115020, https://doi.org/10.1016/j.jelechem.2021.115020.
[60] R.A. Budiman, T. Ishiyama, K.D. Bagarinao, H. Kishimoto, K. Yamaji, T. Horita, Dependence of hydrogen oxidation reaction on water vapor in anode-supported solid oxide fuel cells, Solid State Ionics 362 (2021) 115565, https://doi.org/10.1016/j.ssi.2021.115565.
[61] M. Riegraf, R. Costa, G. Schiller, K.A. Friedrich, S. Dierickx, A. Weber, Electrochemical impedance analysis of symmetrical Ni/gadolinium-doped ceria (CGO10) electrodes in electrolyte-supported solid oxide cells, J. Electrochem. Soc. 166 (13) (2019) F865, https://doi.org/10.1149/2.0051913jes.
[62] A. Solovyev, A. Shipilova, E. Smolyanskiy, S. Rabotkin, V. Semenov, The properties of intermediate-temperature solid oxide fuel cells with thin film gadolinium-doped ceria electrolyte, Membranes 12 (9) (2022) 896, https://doi.org/10.3390/membranes12090896.
[63] H. Wang, Z. Gao, S.A. Barnett, Anode-supported solid oxide fuel cells fabricated by single step reduced-temperature co-firing, J. Electrochem. Soc. 163 (3) (2015) F196, https://doi.org/10.1149/2.03716023jes.
[64] P. Caliandro, A. Nakajo, S. Diethelm, Model-assisted identification of solid oxide cell elementary processes by electrochemical impedance spectroscopy measurements, J. Power Sources 436 (2019) 226838, https://doi.org/10.1016/j.jpowsour.2019.226838.
[65] J.H. Park, S.M. Han, K.J. Yoon, H. Kim, J. Hong, B.K. Kim, J.W. Son, Impact of nanostructured anode on low-temperature performance of thin-film-based anode-supported solid oxide fuel cells, J. Power Sources 315 (2016) 324–330, https://doi.org/10.1016/j.jpowsour.2016.03.055.
[66] K. Huang, M. Feng, J.B. Goodenough, M. Schmerling, Characterization of Sr-Doped LaMnO3 and LaCoO3 as cathode materials for a doped LaGaO3 ceramic fuel cell, J. Electrochem. Soc. 143 (11) (1996) 3630, https://doi.org/10.1149/1.1837262.
[67] A.A. Solovyev, A.V. Shipilova, S.V. Rabotkin, E.A. Smolyanskiy, A.N. Shmakov, Magnetron sputtered LSC-GDC composite cathode interlayer for intermediate-temperature solid oxide fuel cells, Int. J. Hydrogen Energy 47 (89) (2022) 37967–37977, https://doi.org/10.1016/j.ijhydene.2022.08.281.
[68] J.J. Choi, K.S. Cho, J.H. Choi, J. Ryu, B.D. Hahn, W.H. Yoon, D.S. Park, Low temperature preparation and characterization of LSGMC based IT-SOFC cell by aerosol deposition, J. Eur. Ceram. Soc. 32 (1) (2012) 115–121, https://doi.org/10.1016/j.jeurceramsoc.2011.07.036.